Optimization-based Synthesis Of Microresonators

Tamal Mukherjee,[†] Sitaraman Iyer,[†] and Gary K. Fedder[†*]
[†]Department of Electrical and Computer Engineering and [*]The Robotics Institute
Carnegie Mellon University
Pittsburgh, PA, 15213-3890

Abstract

The rapid layout synthesis of microresonators from high-level engineering specifications is demonstrated. Functional parameters such as resonant frequency, quality factor, and displacement amplitude at resonance are satisfied while simultaneously minimizing a user-specified objective function. A synthesis tool implementing the optimization-based formulation can be used to explore micromechanical design issues and objectives, as illustrated with a polysilicon lateral resonator example modeled in three mechanical degrees of freedom. Layouts for four sets of five different resonators from 3 kHz to 300 kHz are generated, with each set globally optimized to minimize either active device area, electrostatic drive voltage, a weighted combination of area and drive voltage, or to maximize displacement amplitude at resonance.

Keywords: CAD, resonator, synthesis

1. Introduction

Layout synthesis provides an automated mechanism for generating valid layout of commonly used micromechanical device topologies from high-level engineering design specifications. This involves both design synthesis and layout generation: design synthesis generates physical layout parameters that can meet the desired device performance, and layout generation translates these physical parameters into a layout description. Prior research on automated layout generation start from user input of the physical layout parameters [1][2], requiring the user to map the design objectives into layout parameters. Although researchers have considered design optimization for simple structures, in which the optimization traded off between a handful of variables [3], we know of no design synthesis approaches, where the entire design is obtained automatically. Our approach is to model the design problem as a formal numerical optimization problem, and then solve it with powerful optimization techniques, resulting in a tool that automates the design synthesis of MEMS structures. Furthermore, we tightly integrate the functional model of the device and its geometrical layout model to aid in the generation of the layout parameters that completely describe the layout. This synthesis philosophy has been successful in a variety of fields such as analog circuit synthesis [4][5] and chemical plant synthesis [6]. The process of modeling the design problem involves determining the design variables, the numerical design constraints, and the quantitative design objective. The resulting optimal synthesis tool enforces codification of all relevant variables and constraints and allows rapid exploration of micromechanical design issues and objectives.

The folded-flexure electrostatic-comb-drive microresonator topology used in this study was first introduced by Tang [7] and is now commonly used for MEMS process characterization. The device has applications in oscillators and high-Q filters [8]. It represents a good starting point for synthesis work since proper operation can be easily verified using existing numerical simulation

tools and experimental measurements. MCNC's surface-micromachined polysilicon Multi-User MEMS Process (MUMPs) and corresponding design rules are used to constrain the design space [9].

Lumped-parameter electromechanical models with three mechanical degrees-of-freedom (in-plane x, y, and θ) link the physical and functional parameters of the microresonator. Building upon our prior synthesis work [10][11][12], we evaluate the effects of four different objective functions and include an additional degree of freedom (in-plane rotation) in the evaluation. The synthesis method can be usefully extended to other micromechanical design topologies as long as the device performances can be evaluated rapidly and with acceptable accuracy.

The next section describes the folded-flexure electrostatic-comb-drive microresonator topology. Section 3 describes the optimization formulation used for the layout synthesis. Section 4 presents the synthesis results, and discusses the validity of the synthesis models. Finally, we conclude in Section 5.

2. Microresonator Description

2.1. Fabrication

A simplified version of the MUMPs technology, chosen for our current synthesis work, is shown in Figure 1. Electrical isolation from the silicon substrate is provided by a low-stress silicon nitride layer, on top of which an electrical interconnect layer of polycrystalline silicon (polysilicon) is then deposited and patterned. Next, a 2 μm-thick sacrificial spacer layer of phosphosilicate glass (PSG) is deposited. After contact cuts are made in the PSG, a 2 μm-thick layer of structural polysilicon is deposited and patterned. Further process steps in MUMPs are not necessary for microresonator fabrication and are not shown. A final wet etch in hydrofluoric acid (HF) dissolves the PSG and releases the microstructures. The PSG contact cuts act as mechanical anchor points that fix the microstructure to the substrate surface [9].

2.2. Layout Topology and Design Variables

A simplified layout of the device is shown in Figure 2. The resonator is a mechanical mass-spring-damper system consisting of a central shuttle mass that is suspended by two folded-beam flexures. The resonator is driven in the preferred (x) direction by electrostatic comb actuators. Assuming that the resonator is operating with a dc voltage V_{dc} applied to the shuttle, and a sinusoidal voltage source with amplitude V_{ac} applied to only one of the actuators, we can simplify the applied voltage as a sinusoidal voltage with amplitude $V = \sqrt{2V_{ac}V_{dc}}$. The suspension is designed to be compliant in the x direction of motion and to be stiff in the remaining degrees of freedom (y and θ) to keep the comb fingers aligned.

The variables needed to describe the layout can be classified as design, style and state variables, as listed in Table I and detailed in Figure 3. Design variables of the microresonator include the comb-drive voltage and sixteen structural parameters of the shuttle mass, folded flexure, and comb drive elements. Technology-driven design rules set minimum beam widths and minimum spaces between structures. Maximum element lengths are constrained to 400 μm to avoid problems with undesirable curling due to stress gradients in the structural film and possible sticking and breakage during the wet release etch [13]. Maximum beam widths are constrained to 20 μm by the limited undercut of PSG to release the structures [9]. The comb yoke is allowed to extend to fill up the entire flexure length allowed for the resonator. Style variables do not affect the resonator behavior, but are necessary to completely define the geometrical layout. These variables are set to fixed values and include the width of the anchor supports, w_{ba} and w_{ca}, the offset of attachment points of the flexure beams to the anchor edge, and the overlap around anchor cuts. State variables are used to simplify design constraints and can be defined as functions of the design variables. For example, the shuttle axle length, L_{cy}, is a state variable which is dependent on the number of fingers (N), finger width (w_c) and air gap (g).

2.3. Modeling

With the definition of the variables completed, we can now develop functional performance models expressed in terms of these variables. We begin by looking at the first four modes of the resonator, depicted in Figure 4. The fundamental lateral resonator mode is always in the x direction to be considered a valid resonator design. The second and third modes alternate between the vibration of the beam flexures and the rotational (θ) mode, depending on the type of design objectives and constraints used. We are only interested in the fundamental and second modes and, therefore, model the x, θ, and flexure modes. (The y-mode is also modeled, however it does not affect the synthesis outcome.) Out-of-plane modes are not dealt with in the present study. Each mode of interest is modeled by a lumped second-order equation of motion. For example, for the x mode:

$$F_{e,x} = m_x\ddot{x} + B_x\dot{x} + k_x x \tag{1}$$

where $F_{e,x}$ is the lateral component of the external electrostatic force generated by the comb drives, m_x is the effective mass, B_x is the damping coefficient, and k_x is the spring constant.

Linear equations for the folded-flexure spring constants are found by using energy methods to find displacement for a unit load on the end of the spring [14]. The effect of spring mass on resonance frequency is incorporated in effective masses for each lateral mode. Effective mass for each mode of interest is calculated by normalizing the total maximum kinetic energy of the spring by the maximum shuttle velocity, v_{max}.

$$m_{eff} = \sum_{beam\ i=1}^{N} \frac{m_i}{L_i} \int_0^{L_i} \left(\frac{v_i(\xi)}{v_{max}}\right)^2 d\xi \tag{2}$$

where m_i and L_i are the mass and length of the i’th beam in the flexure. Analytic expressions for velocities, v_i, along the flexure’s beams are approximated from static mode shapes, and are found from the spring constant derivations.

The full modeling equations for the microresonator in the general case are extremely long and, therefore, are presented in a technical report [15]. Here, we focus on simplified models of the important resonator modes. The spring constant of the fundamental mode is:

$$k_x = \frac{2Etw_b^3}{L_b^3} \frac{L_t^2 + 14\alpha L_t L_b + 36\alpha^2 L_b^2}{4L_t^2 + 41\alpha L_t L_b + 36\alpha^2 L_b^2} \tag{3}$$

where E is the Young's modulus of polysilicon, t is the polysilicon thickness, and $\alpha = (w_t/w_b)^3$. In the limit of infinitely stiff trusses, approximated by $\alpha \gg L_b/L_t$, the effective mass is

$$m_x = m_s + \frac{1}{4}m_t + \frac{12}{35}m_b \tag{4}$$

where m_s is the shuttle mass, m_t is the total mass of all truss sections, m_b is the mass of all long beams. The resonant frequency is given by $\omega_x = 2\pi f_x = \sqrt{k_x/m_x}$. Resonant frequency of the other modes are estimated from corresponding effective mass and spring constant values.

The flexure modes are modeled with the one-dimensional half-resonator system shown in Figure 5. The flexure behavior is lumped into an effective mass, m_{fl}, and a flexure spring, k_{fl}, which is split into an anchored component and a component connected to the shuttle mass. The flexure modal frequency of this system is

$$\omega_{fl} = 2\pi f_{fl} = \sqrt{\frac{k_f}{m_{fl}}\left(1 + \frac{m_{fl}}{2m_s} + \left(\frac{m_{fl}}{2m_s}\right)^2\right)} \tag{5}$$

where, assuming an infinitely stiff truss, the flexure effective mass is

$$m_{fl} = \frac{m_t}{2} + \frac{6}{35}m_b \tag{6}$$

and the flexure spring constant is

$$k_{fl} = 4Et\left(\frac{w_b}{L_b}\right)^3 \quad (7)$$

The symmetric and anti-symmetric flexure modes are degenerate in this one-dimensional approximation. Rotation of the shuttle mass in the anti-symmetric mode is left as future work.

Viscous damping generated by the moving shuttle in air is modeled as Couette flow using equations derived in [16].

$$B_x = \mu\left[(A_s + 0.5A_t + 0.5A_b)\left(\frac{1}{d} + \frac{1}{\delta}\right) + \frac{A_c}{g}\right] \quad (8)$$

where μ is the viscosity of air, d is the fixed spacer gap of 2 m, δ is the penetration depth of airflow above the structure, g is the gap between comb fingers, and A_s, A_t, A_b, and A_c are bloated layout areas for the shuttle, truss beams, flexure beams, and comb finger sidewalls, respectively. Damping factors of the other lateral modes do not enter into the design constraints and are not calculated.

General analytic equations for the lateral comb-drive force, F_x, as a function of w_c, g, structure thickness, and sacrificial spacer thickness are derived in [17]. For the special case of equal comb finger width, gap, thickness, and spacing above the substrate ($w_c = g = t = d$), each comb drive generates a force that is proportional to the square of the voltage, V, applied across the comb fingers.

$$F_{e,x} \cong 1.12\varepsilon_o N \frac{t}{g} V^2 \quad (9)$$

where ε_o is the permittivity of air. If the comb fingers are not perfectly centered, a y-directed electrostatic force is also present. Assuming a small perturbation in y displacement, the destabilizing force, $F_{e,y}$, is proportional to displacement such that $F_{e,y} = k_{e,y}\,y$, where $k_{e,y}$ is an ‘electrical negative spring constant.’

$$k_{e,y} \approx 2.24\varepsilon_o N V^2 (x_o + x) \frac{t}{g^3} \quad (10)$$

Since the stiffness in y is usually very large, the destabilizing electrostatic torque, $\tau_{e,\theta} = k_{e,\theta}\,\theta$, generated by the comb drive becomes the more stringent constraint. The rotational spring constant is found by realizing that the destabilizing force acts through a moment arm, X_c, on the center of the resonator, giving

$$k_{e,\theta} = k_{e,y} X_c^2 \approx 2.24\varepsilon_o N V^2 (x_o + x) \frac{t}{g^3} X_c^2 \quad (11)$$

where $X_c = 0.5\, L_{sa} + w_{cy} + L_c - 0.5\, x_o$.

3. Layout Synthesis

Converting the microresonator layout topology, design variables, and model into an optimization problem that can design the microresonator involves determining the constraints and objectives for the design. We can break the constraints into two classes: geometric and functional. The geometric constraints are layout specific, and therefore vary with topology. The functional constraints refer to the device's function, and remain constant for an entire class of devices (all microresonators have a constraint on resonant frequency).

3.1. Geometric Constraints

The geometric constraints illustrated in Figure 6 are necessary to ensure a functional resonator. The constraints are detailed in Table II. The resonator width and length must not exceed an arbitrary fixed size, set at 700 μm in all of the results presented in this paper. The overall resonator length is determined by either the flexure or comb-drive actuator, therefore both constraints need to be simultaneously satisfied. A linear form of the actuator length constraint was chosen to aid in the efficiency of the optimization-based synthesis (an alternative non-linear form of the constraint would have been $(2N + 1)w_c + 2Ng$). Gaps between the comb fingers and between the shuttle

and beam anchor must allow the shuttle to move freely and must accommodate the maximum possible stroke. The maximum expected displacement of the shuttle mass will be at resonance, and is encoded in the motion limit constraints using x_{disp}. (comb fingers motion limited to prevent crashing, to ensure minimum comb overlap for linear comb-drive actuation and to provide adequate shuttle gap in the x direction). Finally, a shuttle gap constraint is defined to encode the technology-driven design rule for gaps between moving and anchored parts.

In our formulation, all constraints relating actual design variables to state variables must be included. However, for the microresonator topology only one state variable was deemed necessary, L_{cy}, leaving one state-variable related constraint: $(2N+1)w_c + 2Ng \le L_{cy}$. This is to ensure that the comb yoke is wide enough to accommodate all the comb fingers.

3.2. Functional Constraints

Realistic engineering specifications are chosen for synthesizing a valid resonator for use as a characterization structure, and are detailed in Table III. Alternative constraint values can be readily assigned in the implementation.

An essential specification is resonant frequency of the lowest (preferred) mode. Since the resonant frequency is a non-linear function of the variables, we require that the generated layouts have a resonant frequency within ε of the desired frequency, instead of solving for the exact frequency ($\varepsilon = 1\%$ for this study). Resonant frequencies of the other possible second modes, f_{fl} and f_θ, must be greater than f_x to decouple the modes (we use an *ad-hoc* factor of three to ensure mode separation). For stability, the restoring force of the spring in the y direction must be three times greater than the destabilizing electrostatic force from the comb drive (*i.e.,* $3k_{e,y} < k_y$). A similar stability constraint must hold for the rotational mode.

Assuming the system is underdamped, the displacement amplitude at resonance is

$$x_{disp} = QF_{e,x}/k_x, \tag{12}$$

where $Q = \sqrt{m_x k_x / B_x^2}$ is the quality factor, $F_{e,x}$ is the comb-drive force, (9), and B_x is the damping coefficient, (8). We have constrained $x_{disp} = 3$ µm 10% at a drive voltage of $V < 50$ V to enable easy visual confirmation of resonance, and $Q \geq 5$ to ensure underdamped resonant operation.

Some of the lumped-parameter macromodels were derived based on simplifying assumptions. For example, central shuttle axle stiffness should always be dominated by flexure stiffness. This assumption is enforced by constraining $k_{y,\,axle} > 10k_y$. In the x direction, we assume that the flexure stiffness will be linear, which we enforce by $L_b > 10x_{disp}$.

Finite residual stress in mechanical polysilicon films can cause released fixed-fixed suspensions to exhibit non-linear behavior in tension or buckle under compression. Polysilicon can be deposited either compressive or tensile, depending on deposition conditions. In the MUMPs process, residual stress is always compressive, having a nominal value of -10 MPa and worst-case value of -20 MPa [9]. Beams in the folded flexure are free to expand outward to relieve residual axial stress. However, as shown in Figure 7, the central shuttle also expands an amount Δ due to residual stress, creating additional axial stress in the outer beams and tension in the inner beams. A first-order value of the critical buckling length, L_{cr}, for the folded-flexure is given by the Euler column formula, $L_{cr} = \pi w \sqrt{2L_b / 3\Delta}$, where $2L_b < L_{cr}$ to ensure no buckling, and w corresponds to the minimum of w_b and w_c.

Therefore, we have constraints on resonant frequency, stroke at resonance, quality factor, off-axis stability, off-axis decoupling, accuracy and buckling. A summary of the functional constraints on the engineering specifications is given in Table III.

3.3. Design Objective

Our synthesis approach selects the design that minimizes an objective function and therefore may be considered optimal. The synthesized result depends very strongly on the choice of objective function. For the microresonator, we have chosen three objective functions to minimize: total resonator active area, amplitude of the comb-drive voltage, and the sum of active area and drive voltage normalized to the maximum possible area and voltage; and a fourth objective function to maximize: displacement at resonance.

The choice of design objective may affect the earlier constraint choices. The $x_{disp} = 3\ \mu m\ \ 10\%$ constraint described in Section 3.2 is incompatible with the maximize displacement objective, hence we replace it with $x_{disp} > 2\ \mu m$.

3.4. Synthesis Algorithm

In our approach, the synthesis problem is mapped onto a constrained optimization formulation which is solved to generate the device layout. In this approach the constraints and the objective can be evaluated by firing the lumped-parameter macromodels described in Section 2.3 to determine the extent to which the functional constraints are met, for the current values of the design variables. Depending on the choice of the objective function, there can be more than one minimum point in the optimization, due to the complex non-linear characteristics of the individual model equations. Furthermore, since our goal is synthesis, we need to be independent of any choice of starting point for the optimization.

Currently, a gridded multi-start algorithm coupled with a gradient-based constrained optimization efficiently solves for the global minimum of the objective function. The use of a starting grid eliminates the need to provide good starting points to the gradient-based optimization. In addition, the algorithm stores all the local minima reached from the various starting point, and then determines the global minimum, which is returned to the user. Our current implementation uses a loga-

rithmic starting grid, to span the entire domain of the design variables, each of which can vary over a couple of orders of magnitude. This is particularly important for the design objectives that are complicated functions of the design variables, such as maximizing resonator displacement (x_{disp}). For linear design objectives (such as minimizing drive voltage, V) there is only one optimal solution, eliminating the need for the gridded multistart algorithm.

The general non-linear constrained optimization formulation can be written as:

$$\begin{aligned} \min_{\underline{u}} \quad & z = \sum_{i=1}^{\kappa} w_i \cdot f_i(\underline{u}, \underline{x}) \\ \text{s.t.} \quad & \underline{h}(\underline{u}, \underline{x}) = 0 \\ & \underline{g}(\underline{u}, \underline{x}) \le 0 \\ & \underline{u} \in U_P \end{aligned} \tag{13}$$

where $\underline{u}$ is the vector of design variables given in Table I; $\underline{x}$ is the vector of state and style variables; $\underline{f}(\underline{u}, \underline{x})$ is a set of objective functions that codify performance specifications the designer wishes to optimize, *e.g.*, area; and $\underline{h}(\underline{u}, \underline{x}) = 0$ and $\underline{g}(\underline{u}, \underline{x}) \le 0$ are each a set of functions that implement the geometric and functional constraints given in Table II and Table III. For example, resonant frequency is constrained to greater than 20 kHz by the function $20000 - f_x(\underline{u}, \underline{x}) \le 0$ where $f_x(\underline{u}, \underline{x})$ is the lumped-parameter macromodel of the resonant frequency in the x direction. Scalar weights, w_i, balance competing objectives. The design variables can be described as a set $\underline{u} \in U_P$, where U_P is the set of allowable values for $\underline{u}$ (described by the bounds in Table I).

The MEMS design problem cannot be completely modeled in the non-linear constrained optimization formulation. Some of the design variables (such as the number of comb fingers) are integer in nature. Furthermore, all the geometry parameters will eventually detail the physical design in the VLSI masks. Therefore they should be represented as integers with centi-micron units rather than as real numbers, the result of classical non-linear constrained optimization formula-

tion. We use a combination of snap-to-grid at the end of the optimization to handle these geometric size variables and branch-and-bound type algorithms [18] to handle the strongly integer variables such as number of comb fingers.

In our next-generation tool, we plan to use simulated annealing [19] as the optimization engine to drive the search for the minimum; it provides robustness and the potential for combinatorial global optimization in the face of many local minima. Because annealing incorporates controlled hill-climbing, it can escape local minima and is essentially starting-point independent. Furthermore because of its combinatorial nature, we can completely model the integer nature of selected design variables.

4. Results And Discussion

We have implemented the above algorithm into a synthesis tool that automatically generates valid layout from given engineering design specifications. Synthesized layouts are presented, validated against finite-element software, and by fabrication. The synthesis tool is then used for design-space exploration, to highlight the critical constraints affecting the microresonator design.

We have synthesized resonators for four different objective functions as shown in Figure 8 (minimize area, minimize voltage, minimize a combination of area and voltage, and maximize displacement at resonance). We used the Consolidated Micromechanical Element Library (CaMEL) parameterized module generation software [1] to generate CIF output from the layout parameters determined by the synthesis tool. The CaMEL generators automatically place holes in the large plates that are over 30 μm in size.

A synthesis system can be used to aid a designer in the understanding of the design space, as can be seen when we consider the four different objectives mentioned above. In all four objectives we are able to synthesize resonators ranging from 1.6 kHz to 300 kHz. This range is determined by the combination of design variable ranges and nominal process parameters. Each objective,

however, guides the synthesis to explore a different region of the design space, leading to the diverse layouts shown in Figure 8. The three minimization objectives (area, voltage, and combination of area and voltage) are simple functions of the design variables: voltage is itself a design variable, and area is a simple product of design variables. Comparatively, the displacement at resonance is a complicated function of the design variables, as shown in equation (12). We see that the three sets of resonators obtained from the minimization of the simple objective functions all have optimal designs with minimum widths of beams and comb fingers. In comparison, when we consider the design objective of maximizing the displacement at resonance, the beam widths are larger than their minimum values in the middle of the frequency range. This occurs because the displacement (x_{disp}) and beam lengths (L_b) are linked by the k_x accuracy constraint (see Table III), causing the optimization to use longer flexures than those needed for the simpler objectives. For such long flexures, thicker beams were required to ensure adequate stiffness. Furthermore, the minimum area resonators tend to have the fewest fingers, the minimum voltage resonators tend to have the most comb fingers, the minimum sum of area and voltage resonators tend to trade off between fingers and drive voltage. Finally, the maximum displacement resonators tend to have the longest fingers (needed for their large displacements).

The lumped-parameter expressions were verified with finite-element simulation [20] using 2D 8-node plane stress elements to model each resonator. Values of selected lumped-parameter and finite-element modes and all functional constraint values for the maximized displacement family are given in Table IV. The frequency model in the x direction is within 1% to 5% of finite-element results. The lumped-parameter models show that the f_x/f_{fl} and f_x/f_θ frequency ratios are less than 1/3 as demanded by the mode-separation constraint. When the frequency ratio reaches 1/3, the constraint is considered active. We have shaded all values related to active constraints in Table IV. The higher order mode accuracy is about 10% when the respective frequency is active. As active

constraints tend to arise from *ad-hoc* limits (1/3 for mode separation and stability, and 1/10 for accuracy) model inaccuracy can be also handled by more conservative ratios, leading to conservative designs. Our models show good matching for the *x* direction (critical desired operating specification) and adequate matching for higher order modes, as compared with finite-element simulation.

We now proceed to experimental verification of the synthesized resonators. Resonators have been fabricated in MUMPs, and the resonant frequencies in the *x* direction have been measured as shown in Table V. The family of resonators measured had been synthesized for minimum sum of area and voltage. The relative error of the synthesized frequency with respect to the experimentally measured resonant frequencies (shown in Table V) ranges from 22% to 30%, which is higher than the expected accuracy of the *x* direction resonant frequency as validated by the finite-element simulations. This higher than expected error is due to a systematic ~0.3 µm overetch of the structural layer, which causes a significant overestimation of the bending moment of inertia from the rectangular cross-section approximation, particularly for the minimum width 2 µm beams and trusses. Additionally, the measured value of structural film thickness was 1.9 µm instead of the nominal value of 2 µm. These measurements indicate a trapezoidal cross section for the flexure beams. When we refine the lumped-parameter models in the synthesis system to use a trapezoidal cross section as a first-order model of the overetch, the resonant frequencies are within 5% of the measured values, as shown in Table V.

Process variations result in the variation of the functional parameters in fabricated resonators. For example, to first order, a 5% variation in beam width produces a 7.5% variation in resonant frequency. Furthermore, these variations have global and local components. Global variations include overetch variations noted above. Local variations are of critical importance to designers using symmetry to eliminate systematic offsets. For these topologies, the mismatch or local varia-

tion needs to be included. We fully expect that the synthesis results will change on inclusion of these variations. For example, prior knowledge of the overetch variations would have guided the synthesis tool to select larger beam widths, thereby resulting in smaller variations on beam widths. Previously, we have shown that the optimization formulation of an analog circuit design problem can be extended to include process variations, thereby resulting in robust designs [5]. The synthesis approach presented in this paper is readily extensible in that direction, and we plan on including process variations as future work.

Now that we have validated the synthesis approach, we use synthesis to explore the microresonator design space. In particular, we will explore the trade-off between the various functional constraints, which is of significant interest to most designers. We focus on the extreme high and low frequency designs since they tend to involve the maximum number of constraints between which trade-off decisions have to be made.

As expected, the resonators become smaller with increasing values of resonant frequency. Smaller devices have less mass, and smaller flexures are stiffer. Both effects increase the resonant frequency. Parameters directly relevant to the high-frequency limit are plotted in Figure 9 (a). Increasing the resonator frequency requires an increase in stiffness, k_x, which can be accomplished using shorter beams, L_b. This in turn increases the cross-axis stiffness, k_y, and forces the shuttle axle stiffness, $k_{y,axle}$, to follow due to the k_y accuracy constraint. In principle, the axle may be stiffened by decreasing the axle length, L_{sa}, or increasing the axle width, w_{sa}. However, decreasing L_{sa} requires a decrease in the truss beam length, L_t, which reaches its minimum possible value. Increasing w_{sa} is not possible because it leads to increased m_x (high frequency requires reduced mass).

Low-frequency resonators are limited both by the upper bounds imposed on geometry and by excessive damping as illustrated in Figure 9 (b). The maximum flexure length of 700 μm sets a

lower limit on spring constant of around 0.15 N/m. Further reduction in frequency can be obtained by increasing the shuttle mass via larger w_{cy} or increasing L_t. Due to the maximum height constraint of 700 μm, and the larger sensitivity to the shuttle mass, w_{cy} increases, and L_t decreases at the very edges of the design space. However, quality factor decreases with increasing plate mass, due to the air drag over the larger plate area, reaching the minimum acceptable quality factor of 5.

5. Conclusions

Synthesis algorithms have been successfully applied to generate automatic layout of surface-micromachined resonators from engineering specifications. We have formulated the design problem in terms of an constrained optimization problem. In this approach, the engineering specifications were treated as constraints, and an objective function was used to guide the synthesis to the best design as intended by the designer. Optimal synthesis enables automated exploration of the entire design space given specific user-specified engineering constraints, allowing a designer to understand the complex design trade-off inherent to the design problem.

Once a structured design methodology is established for surface-micromachined MEMS, the synthesis techniques may be extended in the future to general parameterized MEMS design.

Acknowledgments

The authors thank Karen Markus and Ramaswamy Mahadevan of MCNC for use of the CaMEL tool. The research effort is sponsored in part by NSF CAREER award MIP-9625471 and by the Defense Advanced Research Projects Agency (DARPA) and Rome Laboratory, Air Force Materiel Command, USAF, under agreement number F30602-96-2-0304. The U.S. Government is authorized to reproduce and distribute reprints for Governmental purposes notwithstanding any copyright notation thereon. The views and conclusions contained herein are those of the authors and should not be interpreted as necessarily representing the official policies or endorsements, either expressed or implied, of DARPA, Rome Laboratory, or the U.S. Government.

References

[1] *CaMEL Web Page*, http://www.mcnc.org/camel.org, MCNC MEMS Technology Applications Center, 3021 Cornwallis Road, Research Triangle Park, NC 27709.

[2] N. R. Lo, E. C. Berg, S. R. Quakkelaar, J. N. Simon, M. Tachiki, H.-J. Lee, and K.S.J.Pister, "Parametrized layout synthesis, extraction, and SPICE simulation for MEMS," *Proc. ISCAS,* Atlanta, GA, 1996, pp. 481-484.

[3] D. Haronian, "Maximizing microelectromechanical sensor and actuator sensitivity by optimizing geometry," *Sensors and Actuators A,* 50 (1995) 223-236.

[4] E. S. Ochotta, R. A. Rutenbar and L. R. Carley, "Synthesis of High Performance Analog Circuits in ASTRX/OBLX," *IEEE Transactions on CAD*, vol. 15, no. 3, (March 1996) pp. 273-94.

[5] T. Mukherjee, L.R. Carley, and R.A. Rutenbar, "Synthesis of Manufacturable Analog Circuits," *Proc. ACM/IEEE ICCAD,* San Jose, CA, USA, November 1994, pp. 586-593.

[6] I. E. Grossmann and D. A. Straub, "Recent Developments in the Evaluation and Optimization of Flexible Chemical Processes," *Proc. COPE-91*, pp 49-59.

[7] W. C. Tang, T.-C. H. Nguyen, M. W. Judy, and R. T. Howe, "Electrostatic Comb Drive of Lateral Polysilicon Resonators," *Sensors and Actuators A*, 21 (1990) 328-31.

[8] C. T.-C. Nguyen and R. T. Howe, "Micromechanical resonators for frequency references and signal processing," *Proc. IEEE Int. Electron Devices Meeting*, San Francisco, CA, 1994, pp. 343.

[9] D. A. Koester, R. Mahadevan, K. W. Markus, *Multi-User MEMS Processes (MUMPs) Introduction and Design Rules*, MCNC MEMS Technology Applications Center, 3021 Cornwallis Road, Research Triangle Park, NC 27709, rev. 3, Oct. 1994.

[10] G.K. Fedder and T. Mukherjee, "Physical Design For Surface-Micromachined MEMS," *Proc. 5th ACM/SIGDA Physical Design Workshop,* Reston, VA, April 1996, pp.53-60.

[11] T. Mukherjee and G. K. Fedder, "Structured Design Of Microelectromechanical Systems," *Proceedings of the 34th Design Automation Conference (DAC '97)*, Anaheim, CA, June 9-13, 1997.

[12] G.K. Fedder and T. Mukherjee, "Automated Optimal Synthesis of Microresonators," *Proc. 9th Intl. Conf. on Solid-State Sensors and Actuators (Transducers '97),* Chicago, IL, June 16-19, 1997.

[13] C. H. Mastrangelo and C. H. Hsu, "A simple experimental technique for the measurement of the work of adhesion of microstructures," in *Technical Digest*, *IEEE Solid-State Sensor and Actuator Workshop*, Hilton Head Island, South Carolina June 1992, pp. 208-212.

[14] J. M. Gere and S. P. Timoshenko, *Mechanics of Materials,* 4th ed., Boston: PWS Publishing Co., 1997.

[15] S. Iyer, T. Mukherjee, G. K. Fedder, "Optimal Synthesis of the Folded-Flexure Comb-Drive Microresonator," Technical Report, Carnegie Mellon University, 1997.

[16] X. Zhang and W. C. Tang, "Viscous Air Damping in Laterally Driven Microresonators," *Sensors and Materials*, v. 7, no. 6, 1995, pp.415-430.

[17] W. A. Johnson and L. K. Warne, "Electrophysics of Micromechanical Comb Actuators," *J. of Microelectromechanical Systems*, v.4, no.1, March 1995, pp.49-59.

[18] R. Garfinkel and G. L. Nemhauser, "Integer Programming," Wiley, New York, 1972.

[19] S. Kirkpatrick, C. D. Gelatt, and M. P. Vecchi, "Optimization by Simulated Annealing," *Science*, vol. 220, no. 4598, May 1983.

[20] *ABAQUS Web Page,* http://www.hks.com, Hibbitt, Karlsson, and Sorensen, Inc., 1080 Main Street, Pawtucket, RI 02860.

Figures

Figure 1: Abbreviated process flow for MCNC's Multi-User MEMS Process service. (a) Cross-sectional view. (b) Top view (layout).

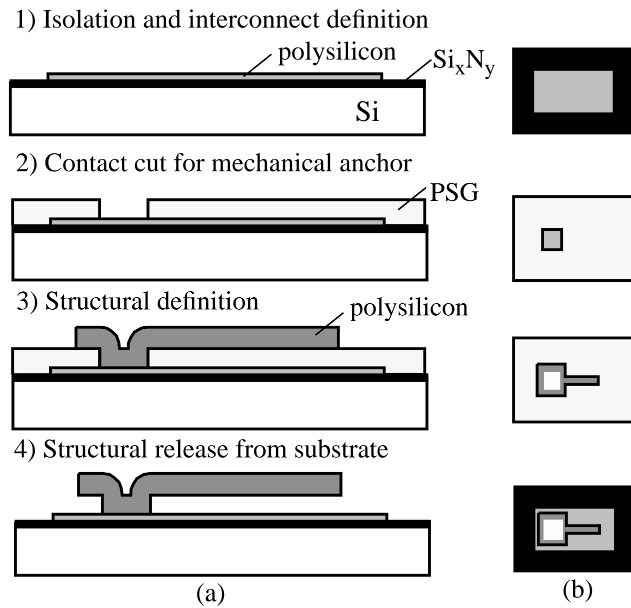

Figure 2: Layout of the lateral folded-flexure comb-drive microresonator.

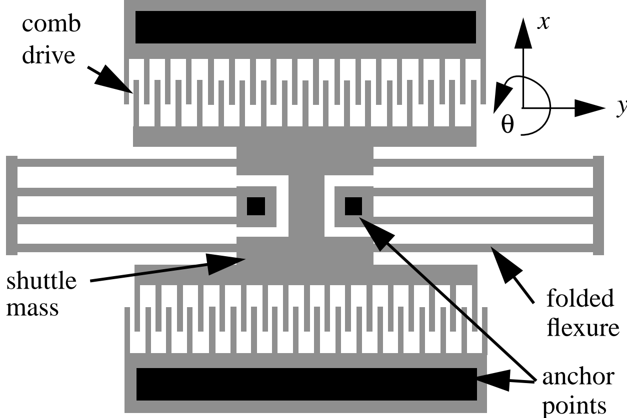

Figure 3: Parameterized elements of the microresonator. (a) shuttle mass, (b) folded flexure, (c) comb drive with N movable 'rotor' fingers, (d) close-up view of comb fingers.

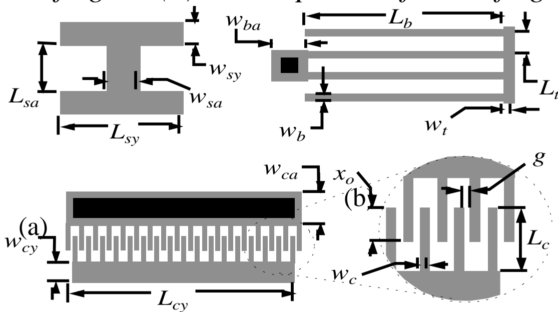

(c) (d)

Figure 4: Finite-element simulation of the first four lateral modes of two representative microresonators. (a) High-frequency case (30 kHz). (b) Low-frequency case (3 KHz).

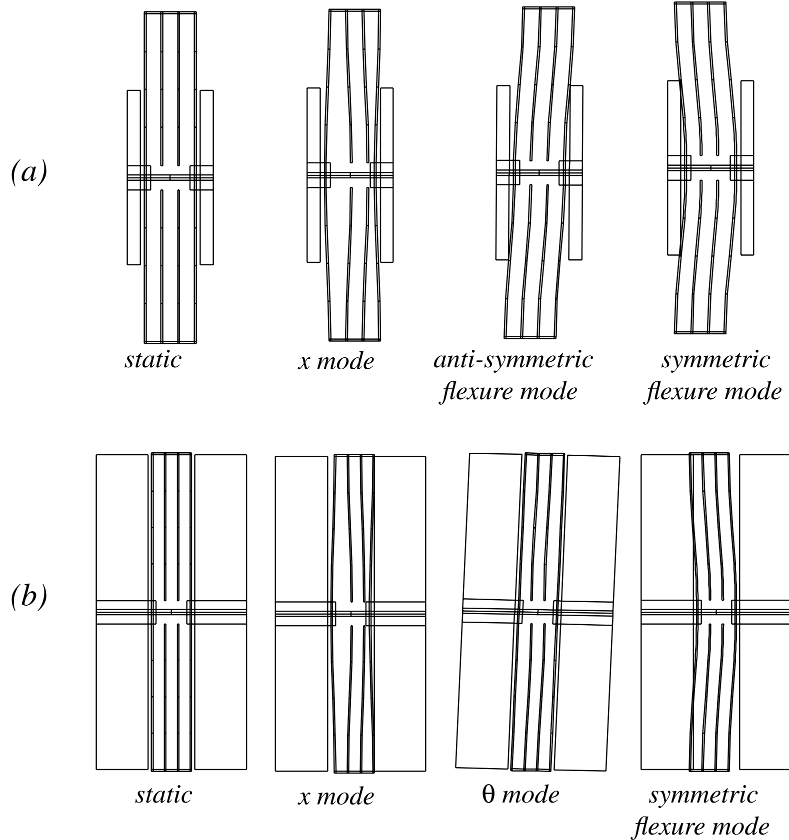

Figure 5: One-dimensional model for determining resonant frequency of the flexure modes, where m_s is the shuttle mass, k_{fl} is the flexure spring constant, and m_{fl} is the flexure effective mass. Only half of the resonator is modeled, taking advantage of symmetry.

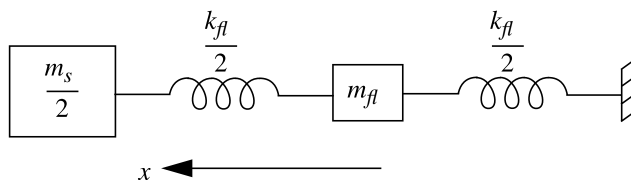

Figure 6: Geometric constraints.

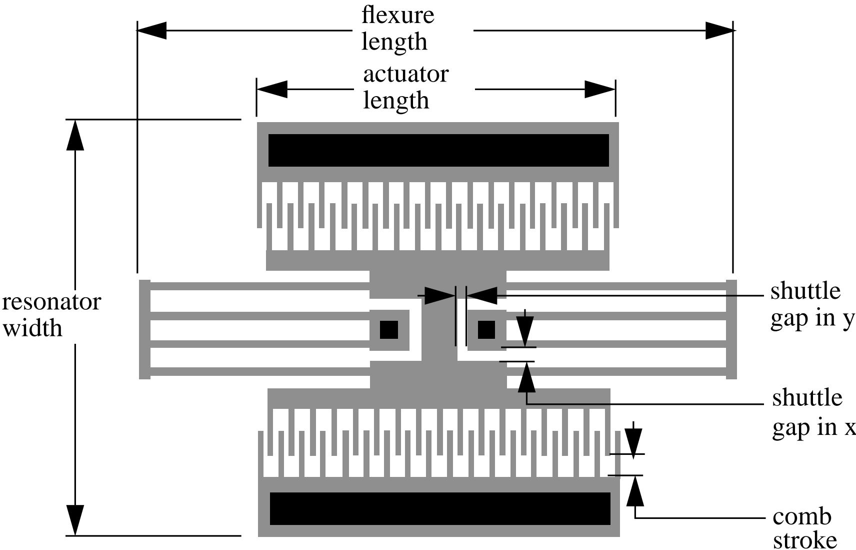

Figure 7: Schematic of the effect of compressive residual stress on the folded-flexure suspension.

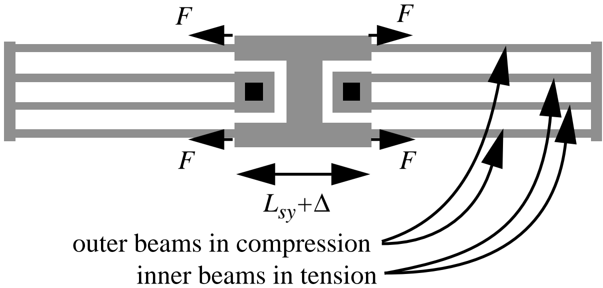

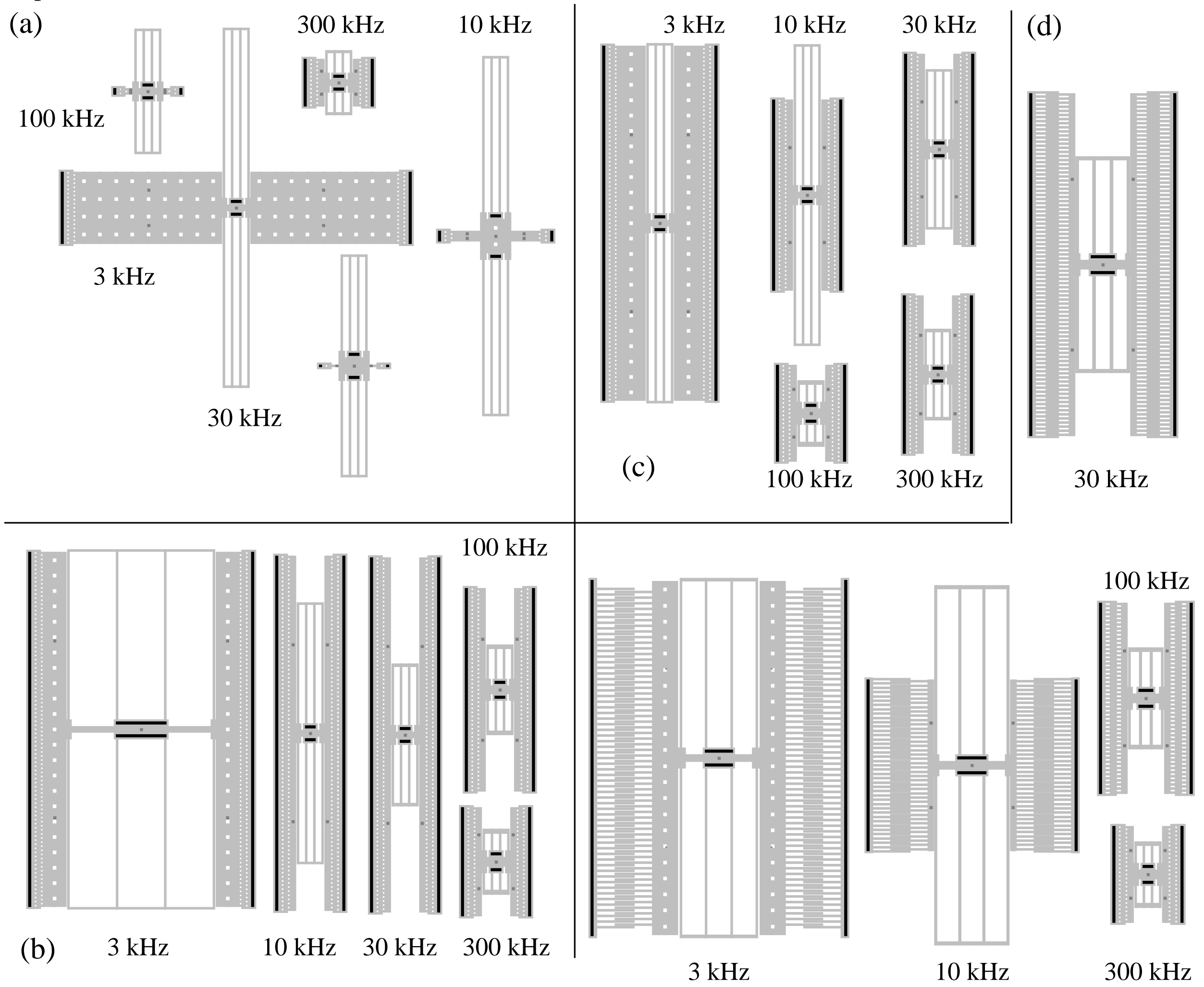

Figure 8: Layout synthesis results for three different objective functions. (a) Minimize active area. (b) Minimize voltage. (c) Minimize normalized sum of area and voltage. (d) Maximize displacement.

Figure 9: Selected design parameters for the synthesized resonators with maximized displacement (dashed lines use right axes, solid lines use left axes). (a) Parameters restricting the high-frequency design space. (b) Parameters restricting the low-frequency design space.

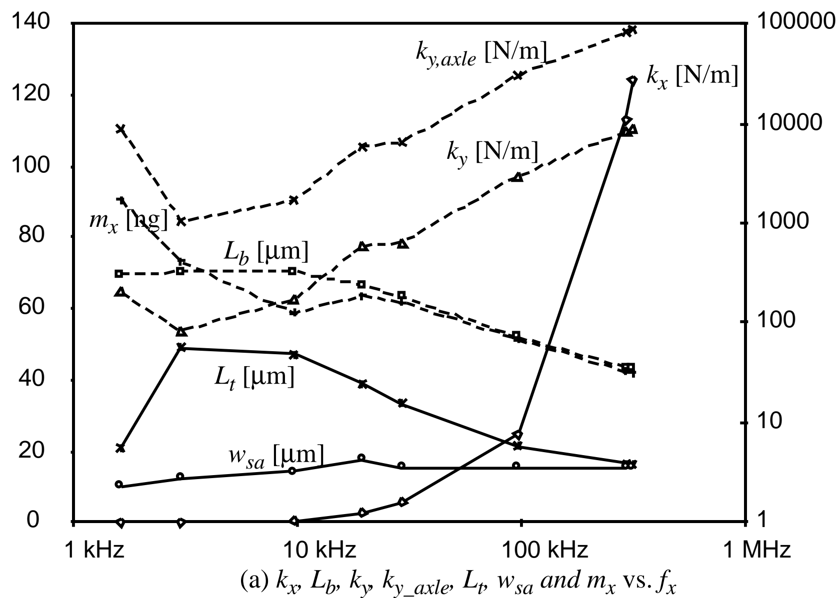

(a) k_x, L_b, k_y, k_{y_axle}, L_t, w_{sa} *and* m_x vs. f_x

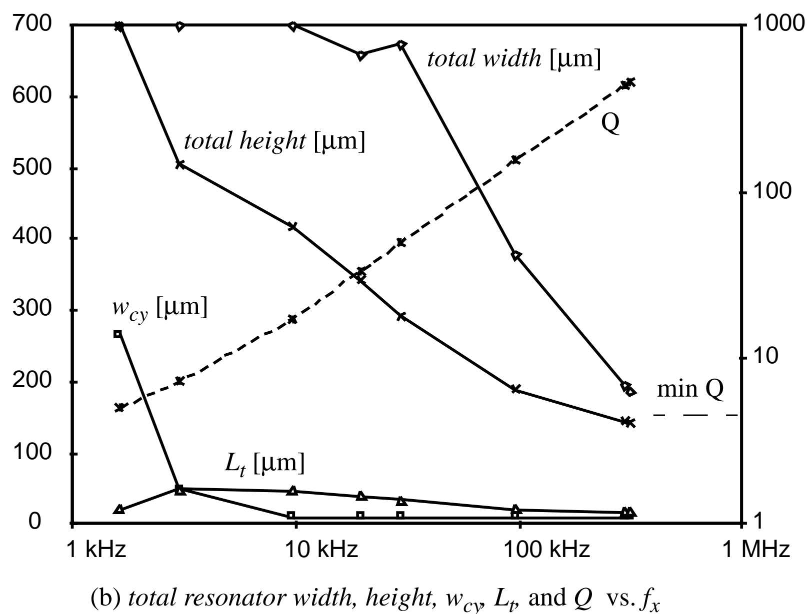

(b) *total resonator width, height,* w_{cy}, L_t, and Q vs. f_x

Tables

TABLE I. DESIGN AND STYLE VARIABLES FOR THE MICRORESONATOR. UPPER AND LOWER BOUNDS ARE IN UNITS OF M EXCEPT N AND V.

var.	description	min.	max.
L_b	length of flexure beam	2	400
w_b	width of flexure beam	2	20
L_t	length of truss beam	2	400
w_t	width of truss beam	2	20
L_{sy}	length of shuttle yoke	2	400
w_{sy}	width of shuttle yoke	10	400
w_{sa}	width of shuttle axle	10	400
w_{cy}	width of comb yoke	10	400
L_{cy}	length of comb yoke	2	700
L_c	length of comb fingers	8	400
w_c	width of comb fingers	2	20
g	gap between comb fingers	2	20
x_o	comb finger overlap	4	400
N	number of rotor comb fingers	1	100
V	voltage amplitude	1 V	50 V
w_{ba}	width of beam anchors	11	11
w_{ca}	width of stator comb anchors	14	14

TABLE II. GEOMETRIC CONSTRAINTS.

Constraint Description	Expression	min [μm]	max [μm]
actuator length	$L_{cy}+2g+2w_c$	0	700
flexure length	$L_{sy}+2L_b+2w_t$	0	700
total resonator width	$3L_t+w_{sy}+4L_c-2x_o+2w_{cy}+2w_{ca}$	0	700
maximum comb stroke	$L_c-(x_o+x_{disp})$	4	200
minimum comb overlap	x_o-x_{disp}	4	200
shuttle gap in x	$L_t-x_{disp}-(w_{sy}+w_b)/2$	8	200
shuttle gap in y	$(L_{sy}-2w_{ba}-w_{sa})/2$	4	200

TABLE III. FUNCTIONAL CONSTRAINTS.

Constraint Description	Expression	min	max
resonant frequency	f_x/f_{xo}	0.99	1.01
stroke at f_x	x_{disp}	2 µm	100 µm
quality factor	Q_x	5	10^5
y-axis stability	$k_{e,y}/k_y$	0	1/3
θ stability	$k_{e,\theta}/k_\theta$	0	1/3
flexure mode decoupling	f_x/f_{fl}	0	1/3
θ decoupling	f_x/f_θ	0	1/3
y decoupling	f_x/f_y	0	1/3
k_y accuracy	$k_y/k_{y,axle}$	0	1/10
k_x accuracy	x_{disp}/L_b	0	1/10
buckling	L_b/L_{cr}	0	1/2

TABLE IV. SELECTED MODEL AND FINITE-ELEMENT SIMULATION VALUES FOR FUNCTIONAL PARAMETERS OF RESONATORS SYNTHESIZED FOR MAXIMIZED DISPLACEMENT HIGHLIGHTING MODEL ACCURACY AND ALL FUNCTIONAL CONSTRAINT VALUES OF RESULTING LAYOUTS[A]. SHADED CELLS INDICATE ACTIVE CONSTRAINTS

f_x Spec[b] (1%)	3 kHz	10	30	100	300
f_x [kHz]	2.99	9.67	29.33	96.59	296.42
$f_{x,\ sim}$ [c] [kHz]	3.03	10.19	29.81	96.40	293.29
f_{fl} [kHz]	33.27	51.96	209.79	669.92	1716.7
$f_{fl,sim}$ [kHz]	32.31	50.56	198.99	636.48	1650.4
f_θ [kHz]	27.50	117.89	89.56	294.02	892.07
$f_{\theta,sim}$ [kHz]	25.42	137.32	82.47	262.29	804.46
Stroke at f_x [μm]	33.3	33.7	18.7	7.3	2.3
Quality factor	7.2	17.2	49.3	155.9	434.2
$k_{e,y}/k_y$ stability	0.09	0.15	0.07	0.01	0.01
$k_{e,\theta}/k_\theta$ stability	0.32	0.33	0.28	0.02	0.01
f_x/f_{fl} decoupling	0.09	0.19	0.14	0.14	0.17
f_x/f_θ decoupling	0.11	0.08	0.33	0.33	0.33
f_y/f_x decoupling	0.04	0.06	0.10	0.09	0.12
$k_y/k_{y,axle}$ accuracy	0.08	0.10	0.10	0.10	0.10
x_{disp}/L_b accuracy	0.10	0.10	0.10	0.10	0.06
L_b/L_{cr} buckling	0.34	0.24	0.14	0.14	0.12

a. Constraint min and max shown in Table III.

b. Synthesized frequency constrained to be within 1% of desired frequency.

c. Rows indicated with sim subscript are results of finite-element simulation

TABLE V. DESIRED, SYNTHESIZED, EXPERIMENTAL AND TRAPEZOIDAL X-SECTION RESONANT FREQUENCIES

f_x Spec[a] (10%) [kHz]	10	30	100	300
Synthesized (square x-section model) $f_{x,syn}$ [kHz]	9	27	90	270
Experimental $f_{x,ex}$ [kHz]	6.9	21	74	210
Rel. err. $\left\lvert\frac{f_{x,syn} - f_{x,ex}}{f_{x,ex}}\right\rvert$	30%	29%	22%	29%
Trapezoidal x-section model $f_{x,trap}$ [kHz]	7.3	21.3	71.6	216
Rel. err. $\left\lvert\frac{f_{x,trap} - f_{x,ex}}{f_{x,ex}}\right\rvert$	6%	1%	3%	3%

a. Synthesized frequency constrained to be within 10% of desired frequency.

List of Figures

Figure 1, "Abbreviated process flow for MCNC's Multi-User MEMS Process service. (a) Cross-sectional view. (b) Top view (layout).," on page 19

Figure 2, "Layout of the lateral folded-flexure comb-drive microresonator.," on page 20

Figure 3, "Parameterized elements of the microresonator. (a) shuttle mass, (b) folded flexure, (c) comb drive with N movable 'rotor' fingers, (d) close-up view of comb fingers.," on page 21

Figure 6, "Geometric constraints.," on page 24

Figure 4, "Finite-element simulation of the first four lateral modes of two representative microresonators. (a) High-frequency case (30 kHz). (b) Low-frequency case (3 KHz).," on page 22

Figure 5, "One-dimensional model for determining resonant frequency of the flexure modes, where ms is the shuttle mass, kfl is the flexure spring constant, and mfl is the flexure effective mass. Only half of the resonator is modeled, taking advantage of symmetry.," on page 23

Figure 7, "Schematic of the effect of compressive residual stress on the folded-flexure suspension.," on page 25

Figure 8, "Layout synthesis results for three different objective functions. (a) Minimize active area. (b) Minimize voltage. (c) Minimize normalized sum of area and voltage. (d) Maximize displacement.," on page 26

Figure 9, "Selected design parameters for the synthesized resonators with maximized displacement (dashed lines use right axes, solid lines use left axes). (a) Parameters restricting the high-frequency design space. (b) Parameters restricting the low-frequency design space.," on page 27

List of Tables

Table I, “. Design and Style variables for the microresonator. Upper and lower bounds are in units of m except N and V.,” on page 28

Table II, “. Geometric Constraints.,” on page 29

Table III, “. Functional Constraints.,” on page 30

Table IV, “. Selected model and finite-element simulation values for functional parameters of resonators synthesized for maximized displacement highlighting model accuracy and all functional constraint values of resulting layouts. Shaded cells indicate active constraints,” on page 31

Table V, “. Desired, Synthesized, Experimental and Trapezoidal X-section resonant frequencies,” on page 32

Author Biographies

Tamal Mukherjee is a Research Engineer and Assistant Director of the Center for Electronic Design Automation in Electrical and Computer Engineering Department at Carnegie Mellon University. H e received his B.S., M.S. and Ph.D. degrees from Carnegie Mellon University in 1987, 1990, and 1995 respectively. His research interests include CAD tools to support analog circuit design and MEMS design, as well as numerical optimization algorithms.

Sitaraman Iyer is a graduate student at the Electrical and Computer Engineering Department at Carnegie Mellon University. He received his B. Tech. degree in Electrical Engineering in 1996 from the Indian Institute of Technology at Mumbai. His research interests include CAD for microelectromechanical systems.

Gary Fedder joined the faculty of Carnegie Mellon University in October 1994 as an Assistant Professor holding a joint appointment with the Electrical and Computer Engineering Department and the Robotics Institute. He received the B.S. and M.S. degrees in electrical engineering from MIT in 1982 and 1984, respectively. From 1984 to 1989, he worked at the Hewlett-Packard Company on circuit design and printed-circuit modeling. In 1994, he received the Ph.D. degree from U. C. Berkeley, where his research resulted in the first demonstration of multimode control of a underdamped surface-micromachined inertial device. He received the 1993 AIME Electronic Materials Society Ross Tucker Award, the 1996 Carnegie Institute of Technology G.T. Ladd Award, and the 1996 NSF CAREER Award. His present research interests include microsensor and microactuator design and modeling, integrated MEMS manufactured in standard CMOS processes, and structured design methodologies for MEMS.